International Micro Air Vehicle Conference and Flight Competition (IMAV2013)
17-20 September 2013, Toulouse, France

Propeller Location Optimisation for Annular Wing Design

Matthew Anderson[1,2], Kai Lehmkuehler[1], Derrick Ho[1],
KC Wong[1] and Patrick Hendrick[2]

[1] The University of Sydney, Sydney, Australia
[2] Université Libre de Bruxelles, Brussels, Belgium
Matthew.Anderson@ulb.ac.be

Abstract

Most research today into the aerodynamics of ducts seeks to increase the thrust or efficiency of a propeller nested inside. This study takes a different approach to duct design and instead examines the use of a duct as an annular wing with the primary function of generating lift for high speed, cruising flight. The variables of investigation for this research are the location of the propeller inside the annular wing and how the thrust generated by the propeller effects the performance of the wing at various angles of attack. This investigation utilises wind tunnel testing to measure the forces generated by the wing and computational fluid dynamics to study the nature of the flow. The results show little difference aerodynamically between fore and aft mounting locations for the propeller in non-stalled flight, however, a forward mounted propeller is shown to be preferable when the flight envelope also includes the stalled regime. In hover, the aft propeller is shown to be favourable.

Contents

1 Introduction

Annular wing aerodynamics (Figure 1 for notations), especially at low Reynolds numbers, is not a widely studied topic. Ribner [13] established the first firm basis for annular wing theoretical modelling, though the advantages of non-planar platforms were known much earlier from the works of Munk [7] and Prandtl [12]. Fletcher [3] conducted wind tunnel tests on five Clark Y profiled annular wings of differing aspect ratios from 0.33 to 3.0, providing one of the first experimental validations of the previous theoretical work of Ribner. Traub [17] furthered this by conducting experiments on two annular wings of aspect ratio 1.0 and 2.0, modifying the existing equations of Ribner for lift slope to take into account aspect ratio, as opposed to using two different equations for high and low aspect ratios. A further model was recently proposed by Maqsood and Go [6] that estimates the performance of annular wings using the leading-edge suction analogy.

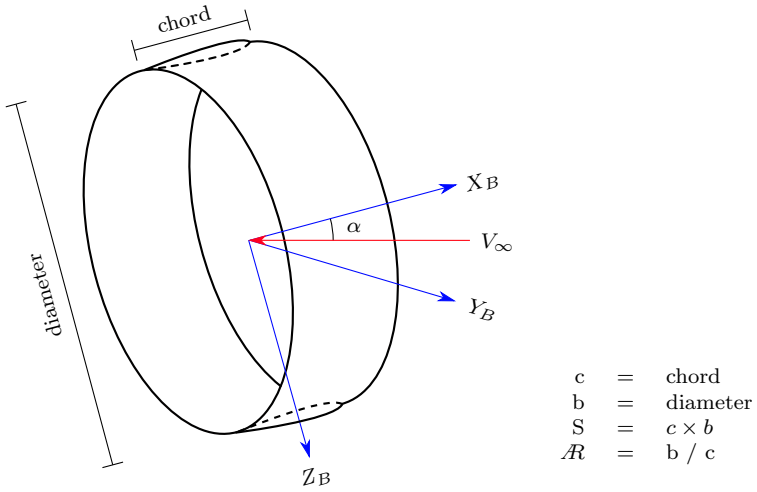

Figure 1: Annular Wing Notation.

The first to prove the advantages of ducted propellers experimentally was Stipa in 1931, and the concept grew in popularity with the development of VTOL and hover capable aircraft [14]. Today, their prevalence is only increasing, especially in the widely studied field of single ducted fan UAVs. Parlett [11] studied the effects of lip diameter, propeller rotation speed and Reynolds number and found that an increasing lip diameter increases the static thrust efficiency. Graf, Fleming and Ng [4] further studied the effects of lip diameter and found that though a larger lip radius enhanced thrust production in static conditions, a smaller lip radius performed more favourably in forward flight and in crosswind conditions. Yilmaz, Erdem and Kavsaoglu [18] investigated the effects of five different duct shapes and found the ducts could provide better propulsive efficiencies, observing up to 10 % efficiency increases, and the duct increased propulsive efficiency up until an advance ratio of 0.3. Their work also showed that a poorly designed duct, in this case only by varying the leading edge of the duct, could adversely affect the performance of the propeller. Sacks [14] notes that little work has been conducted on the position of the propeller within the duct, though he also states that the effect of propeller location could vary significantly in two different duct designs. A later theoretical study by Kriebel, Sacks and Nielsen [5] predicted that the position of the propeller has little effect on the performance of the duct in steady forward flight and hover.

2 Verification of Annular Wing Theory

Experimental investigations on annular wings have shown that theory, when correctly applied, can reasonably predict the lift slope of an annular wing. Experimental span efficiencies have been somewhat varied, although are consistently higher than those achieved by traditional planar wings.

Figure 2 shows a comparison of the theoretical models and wind tunnel experiments found in literature for the lift slope of annular wings [3, 6, 17]. Additionally, calculations using AVL [2] in the spirit of Traub [17] have also been included as a performance prediction method. While there is no 'one size fits all' analytical model for accurately predicting the lift slope, Traub's modified equation presents the best overall analytical prediction method, especially for aspect ratios of two and above. For lower aspect ratios, both the methods from Maqsood and Go and Lowry and Polhamus give very similar results, predicting the lift slope very well. AVL provides the best prediction method, though it is not a simple case of 'plug and play,' and requires some skill on the user end for correct utilisation.

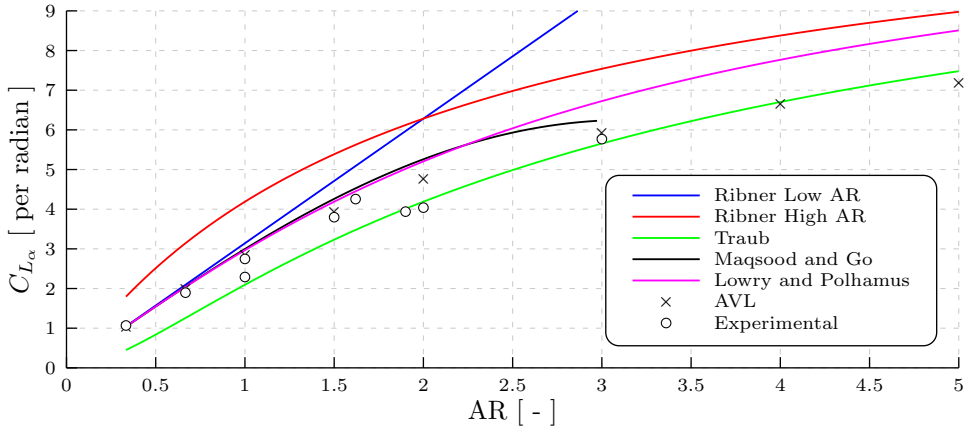

Figure 2: A Comparison of the Theoretical Models for Lift Slope and Wind Tunnel Experiments. Models from [2, 6, 13, 17], additional experimental data from [3, 6, 17].

Classically, the induced drag coefficient for annular wings is modelled as

$$K = \frac{1}{\pi \ AR \ e} \tag{1}$$

where the span efficiency, e, is two. Maqsood and Go proposed an alternate modelling of K such that

$$K = a \left(AR\right)^b \tag{2}$$

where a and b are curve fitted to existing data and equal 0.15 and -1.237 respectively. Equating Equations 1 and 2, the effective e as calculated by Equation 2 is found to be

$$e = \frac{1}{a \ \pi \ AR^{b+1}} \tag{3}$$

which causes some aspect ratio dependence on the span efficiency. Figure 3 shows a comparison of the theoretical models and wind tunnel experiments for span efficiency. Span efficiency is very sensitive to where the the induced drag is considered proportional to the lift squared, and the inherent inaccuracies of digitising data from graphs also affects the calculated value, thus it is very difficult to

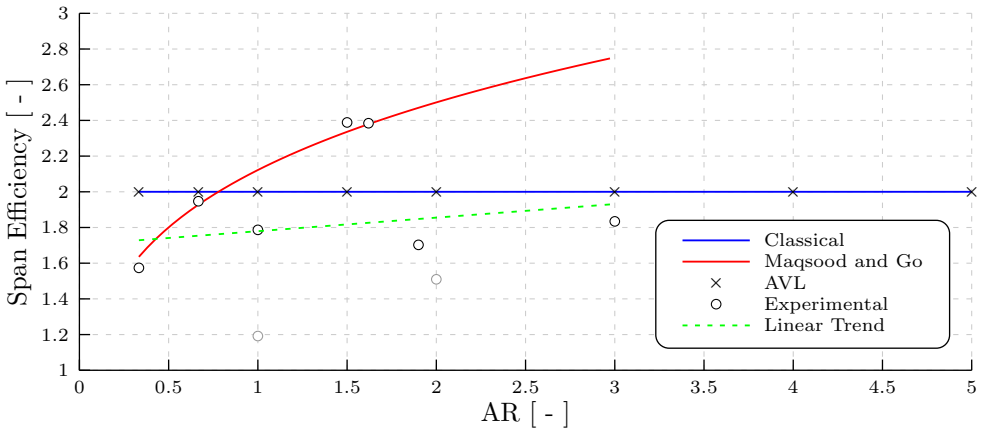

Figure 3: A Comparison of the Theoretical Models for Span Efficiency and Wind Tunnel Experiments. Models from [2, 6, 17], additional experimental data from [3, 6, 17].

get a definitive value from a data set. Nonetheless, the data tends to show values of around 1.8 being achieved experimentally, with little to no dependency on aspect ratio. The span efficiencies of Traub's data (the two greyed out data points) are lower than would be expected, though Traub theorises that this is most likely due to the mounting method of the the model in the wind tunnel.

3 Experimental Set-up

The experimental model (Figure 4) was fabricated using a Rapman Touch 3D printer using ABS plastic and finished to produce a smooth surface. The annular wing has a radius of 152 mm and a chord of 160 mm, giving an overall aspect ratio of 1.9. The aerofoil section is a NACA0012 and causes a slightly divergent inside section due to the aerofoil shape. The central hub section has a radius of 25.5 mm with a straight cylindrical section of 120 mm. The central hub is connected at the quarter chord point of the wing using three NACA0030 profile struts with a chord length of 20 mm.

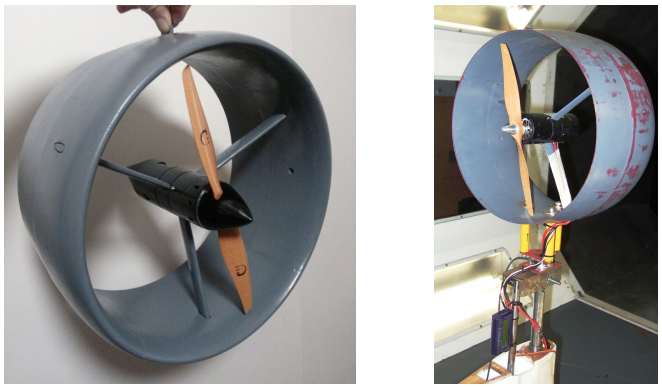

(a) Tractor Configuration (b) Pusher Configuration

Figure 4: The Wind Tunnel Model with the Propeller Mounted in the Tractor and Pusher Positions

The propeller is an 11x5 XOAR and can be mounted 20 mm from the leading edge of the wing for the tractor configuration, or 20 mm from the trailing edge of the wing for the pusher configuration. The clearance between the propeller and the wing is 2.9 % of the propeller radius for the tractor configuration and 6.8 % for the pusher configuration (due to the differing aerofoil thickness at each location). In order to calculate the forces of the wing and hub, thus excluding those of the propeller, the base drag as measured at zero angle of attack was assumed constant in each case, and any differences were attributed to the propeller and subtracted from the total forces. Two tests were run for each case, one at thrust equal to drag, 140 W for the pusher, 165 W for the tractor, and one at 300 W for both the pusher and tractor.

The wind tunnel experiments were conducted in the University of Sydney's '7x5' wind tunnel at 20 m.s^{-1}, corresponding to a Reynolds number of 1.94×10^5. The measured forces were corrected using the method from Shindo [15] and the downwash correction constants used were from Barlow, Rae and Pope [1]. Measurements were taken from -9 degrees in steps of 0.5 degrees until just after stall. The measurement accuracy of the load cell is ± 0.25 N, corresponding to a C_L and C_D error of 0.021, and there is a ± 0.5 degree measurement accuracy in the angle of attack. The values that were obtained in the '7x5' wind tunnel were also verified against earlier testing in the University of Sydney's '4x3' wind tunnel.

4 Computational Fluid Dynamics Set-up

NUMECA FINE/Open with OpenLabs was used to model the wing and propeller set-up. The mesh consists of 2.6M cells and was generated using NUMECA Hexpress to create a fully hexahedral unstructured mesh. Only half the domain was modelled to save computational time and CPU booster and preconditioning were enabled to improve convergence times[1]. The Spalart-Allamaras (Extended Wall Function) turbulence model was used, and the boundary conditions for the turbulence were set from the recommendations of Spalart and Rumsey [16]. The perfect gas model for air was used to allow for compressibility effects and help the stability of the actuator disk. The boundaries were modelled as a velocity inlet / static pressure outlet system, enabling the effects of the propeller to be correctly modelled at the boundaries [9].

The propeller model used is a modified version of the actuator propeller model used by NUMECA's FINE/Marine package, implemented into FINE/Open using OpenLabs. The axial force profile is modelled such that

$$f_{b_{axial}} = \frac{105\ T\ \left(R_h/R_p - r/R_p\right)\left(R_h^2 - R_p^2\right)\sqrt{1 - \frac{R_h/R_p - r/R_p}{R_h/R_p - 1}}}{8\ R_p^2\ \left(3\ R_h/R_p + 4\right)\left(R_h/R_p - 1\right)^2} \tag{4}$$

where T is the desired thrust, R_p is the propeller radius, R_h is the hub radius, and r is the radial distance. The FINE/Marine propeller model also includes the ability to model the tangential force of the propeller such that

$$f_{b_{tangential}} = \frac{105\ Q\ \left(R_h/R_p - r/R_p\right)\left(R_h^2 - R_p^2\right)\sqrt{1 - \frac{R_h/R_p - r/R_p}{R_h/R_p - 1}}}{8\ r\ R_p^2\ \left(3\ R_h/R_p + 4\right)\left(R_h/R_p - 1\right)^2} \tag{5}$$

where Q is the torque and the other coefficients are as in Equation 4 [8]. These forces are then normalised by the volume of the actuator disk and are added into the appropriate momentum equations.

[1]Initial computational investigations on a full mesh showed that modelling the tangential force had little effect on the final total forces, thus were considered negligible and were not included in the final calculations.

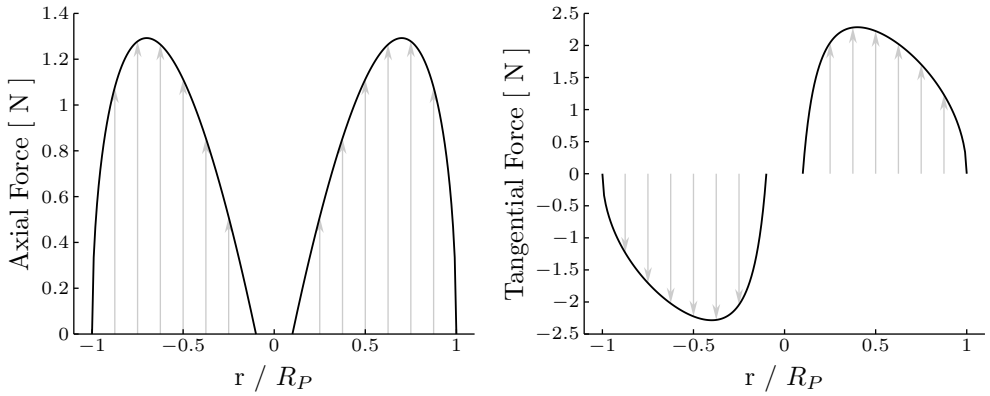

Figure 5: Axial and Tangential Forces for the Modified FINE/Marine Propeller Model

The loading profiles are given in Figure 5 for a propeller of $R_p = 1.0$ m, $R_h = 0.1$ m, $T = 1.0$ N and $Q = 1.0$ N.m. The OpenLabs implementation of the propeller model was verified against Froude's Propeller Theory in a standalone case to ensure the forces were correctly applied. For the computational investigation, three thrusts were investigated, 0.0 N, 2.5 N and 5.0 N, for both configurations.

5 Results

5.1 Experimental Set-up Verification

The results for the wing-only experimental tests (Figure 6) show good agreement with previous experimental data found in literature, verifying the experimental set-up ($\mathcal{R}1.9$ data point in Figures 2 and 3). The lift slope is a lower than would have been expected, though this is most likely due to Reynolds number effects. The span efficiency for the wing-only is 1.7, while low, is within the expected range.

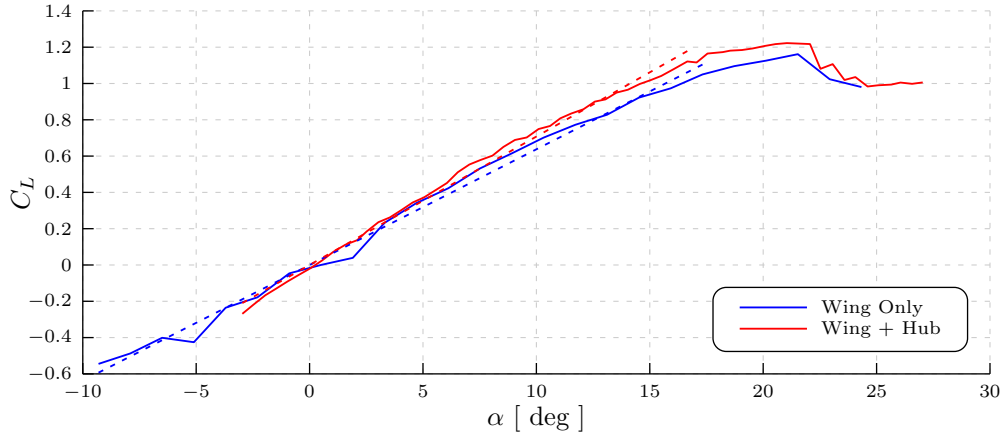

Figure 6: Coefficient of Lift for the Wing-Only and Wing and Hub Configurations. Trendlines dotted, Re $= 1.94 \times 10^5$.

Adding the hub causes the experimental lift slope to increase slightly. The base drag significantly rises, though this is to be expected with the addition of a large body in the middle of the wing. The span efficiency is lowered dramatically by the addition of the hub to around 1.35. Finally, the neutral point shifts aft from $0.42c$ for the wing-only case to $0.68c$ for the wing and hub configuration.

5.2 Effect of Propeller Location

Figures 7 and 8 show the effect of the propeller at different power settings and locations on the lift and drag coefficients. Below stall, little effect is seen on the lift generated by the wing in any of the cases. There is slightly more effect on the drag characteristics, especially at higher power settings. The span efficiency is reduced for the tractor configuration, though the pusher configuration appears to have negligible effect on span efficiency. Interestingly, the power required to equalise thrust and drag at zero angle of attack for the pusher was lower than that for the tractor (140 W versus 165 W), resulting in 1.9 N and 2.2 N of generated thrust respectively. At 300 W, the pusher configuration produces 5.7 N of thrust, compared to the slightly lower 5.4 N for the tractor configuration.

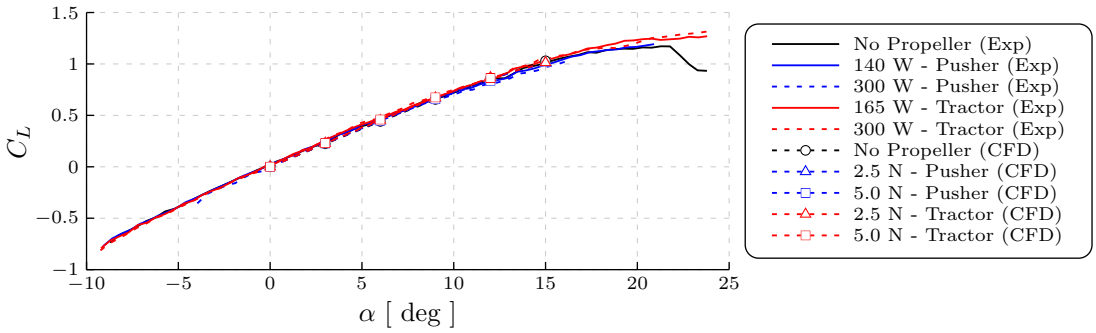

Figure 7: Experimental Lift Coefficient with Thrust Forces Removed and Computational Fluid Dynamics Lift Coefficient. $\mathrm{Re} = 1.94 \times 10^5$.

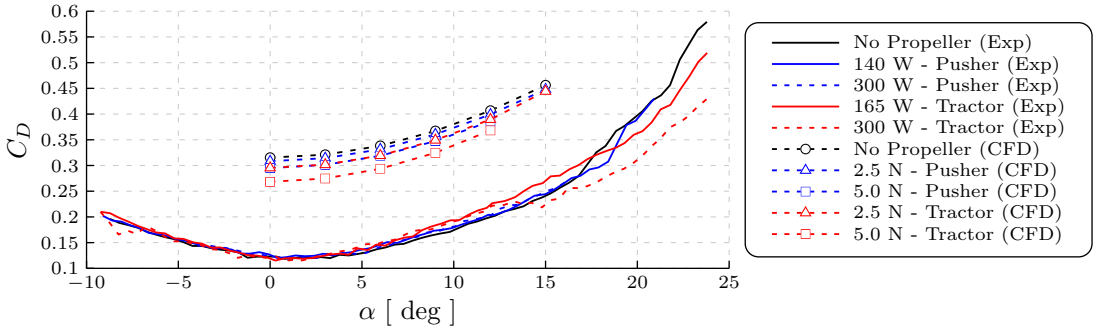

Figure 8: Experimental Drag Coefficient with Thrust Forces Removed and Computational Fluid Dynamics Drag Coefficient. $\mathrm{Re} = 1.94 \times 10^5$.

Computational fluid dynamics (CFD) is shown to be able to predict the lift slope of the configurations very well below stall. While the base drag is not predicted correctly, the induced drag predicted

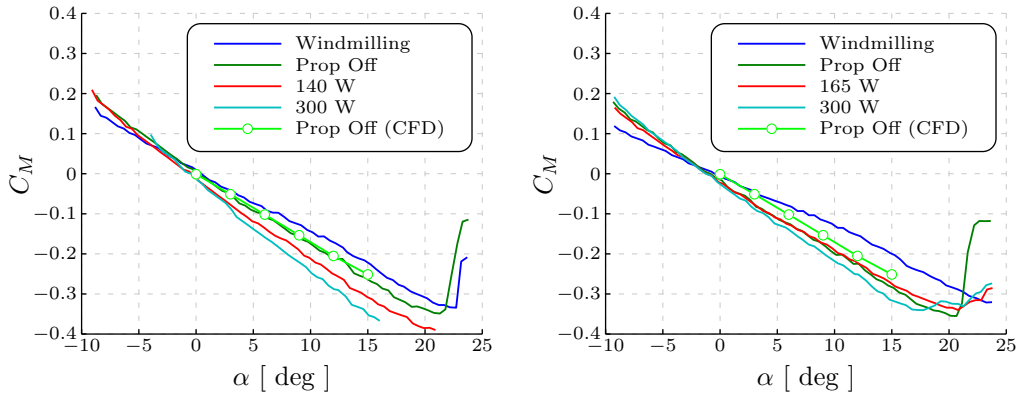

(a) Pusher (b) Tractor

Figure 9: Pitching Moment Coefficient Variation with Propeller Increasing Power about 0.43c. $\mathrm{Re} = 1.94 \times 10^5$.

by CFD follows the experimental results. Futhermore, CFD suggests that the thrust from the propeller causes the base drag of the wing to decrease, especially in the tractor configuration. This can be attributed to the higher speed flow through the wing causing a low pressure region on the lip of the wing [10]. One important point of note is that the experimental results are conducted at a constant power, allowing for some change in generated thrust, while the CFD results are at a constant thrust. As such, the CFD provides an 'ideal' view of how the forces change with the propeller, whereas the experimental results give more of an idea of how this changes in the real world.

As the wing approaches and enters stall, larger variations between the configurations begin to show. The flow forced through the wing by the tractor configuration helps to delay stall by re-energising the boundary layer, increasing $C_{L_{max}}$ to 1.22 (from 1.05 for the no prop configuration) for the low power case. The pusher configuration does delay stall marginally as well, increasing $C_{L_{max}}$ to 1.12, though is far less effective than the tractor configuration. The 300 W case experienced heavy vibration at stall, and the $C_{L_{max}}$ gains at the lower power settings were heavily reduced or disappeared with increasing power. Stall has a greater effect on the pusher cases because the flow separation off the wing hits the propeller, causing a high degree of uneven loading, resulting in reduced propeller effectiveness and increasing vibration. The tractor propeller is in front of this separated flow, and thus doesn't suffer to the same degree as the pusher configuration in stalled flow.

5.3 Effects of Varying Thrust

Figure 9 shows the effect of increasing the thrust produced by the propeller on the pitching moment. As the propeller thrust is increased, the magnitude of the pitch moment slope increases, indicating the wing's neutral point shifts aft. Interestingly, the reverse happens for the windmilling case, shifting the neutral point forward. This is more pronounced for the pusher configuration, indicating that propeller suction has more of an effect on this phenomena than propeller slipstream.

5.4 The Effect of Windmilling

Windmilling causes the propeller to take energy out of the air, resulting in a force acting in the opposite direction to the powered cases. The 'thrust' was calculated as before, and was found to be

-1.9 N for the pusher and -2.5 N for the tractor. Subtracting this force from the recorded forces results in little change in the below stall C_L and C_Ds from the unpowered wing, much like for the powered cases. Windmilling also causes a decrease in the $C_{L_{max}}$, reducing it to 1.00 (from 1.05) in both cases. The violent stall behaviour experienced in the powered tests was also present in the windmilling tests, and was particularly strong for the pusher configuration.

5.5 Static Thrust Tests

Figure 10 shows the net static thrust (as for a hover flight condition) of the pusher and tractor configurations at several power settings. Though the tip clearance is higher for the pusher configuration, it appears to generate around 7 % more thrust at 300 W. This is possibly due to the wing acting as a guide vane, providing cleaner airflow into the propeller. Unlike the tractor configuration, the pusher propeller also sits behind the hub mounting arms resulting in no slipstream blockage.

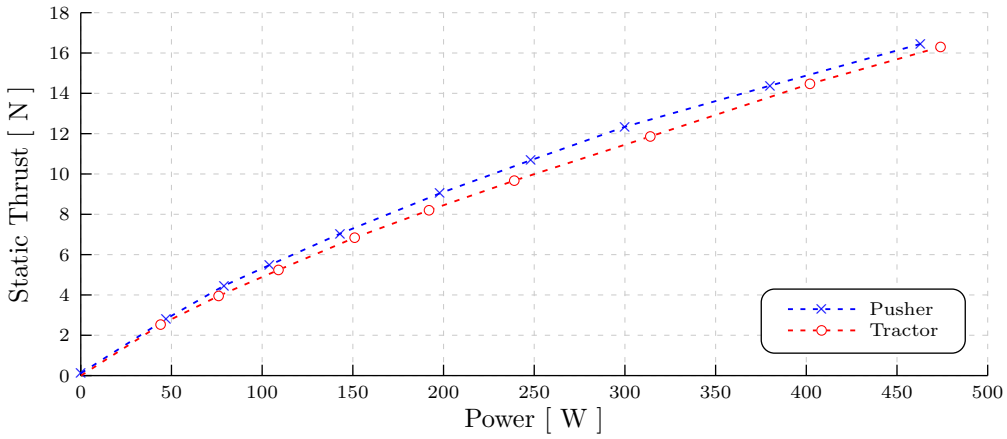

Figure 10: Net Static Thrust Comparison between Pusher and Tractor Configurations. Re = 1.94×10^5.

5.6 Flow Visualisation using Computational Fluid Dynamics

Computational fluid dynamics allows a constant amount of thrust to be applied, regardless of the incoming flow. This allows for the study of the forces over the wing regardless of propeller performance. This is in contrast to the experimental investigation which was carried out with constant propeller power, which allows for some degree of varying thrust.

Figure 11 shows the magnitude of the velocity at a cut through the ZX plane of the wing at 9 degrees angle of attack and in non-stalled flow. Though the tractor propeller sits at the front of the wing, it experiences uneven loading between the top and bottom of the sweep due to the influence of the wing on the airflow (Figure 11a). This causes a decrease in effectiveness of the propeller to generate thrust, and can also cause unwanted vibrations in the aircraft. For the pusher configuration, by the time the air reaches the propeller at the back of the wing (Figure 11b), it has become much more uniform, allowing the propeller to generate thrust far more efficiently. In addition to this, the boundary layer is well developed when it reaches the pusher propeller, which reduces the effective gap between the wing and the propeller, reducing tip vortices leading to lower power consumption.

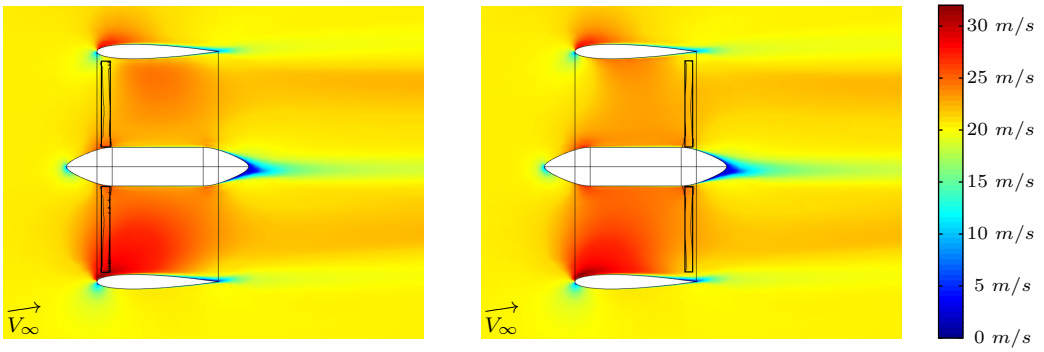

(a) Tractor (b) Pusher

Figure 11: Magnitude of the Velocity for the Tractor and Pusher Configurations in Non-Stalled Flow. Angle of Attack = 9 deg, T = 2.5 N, Re = 1.94×10^5.

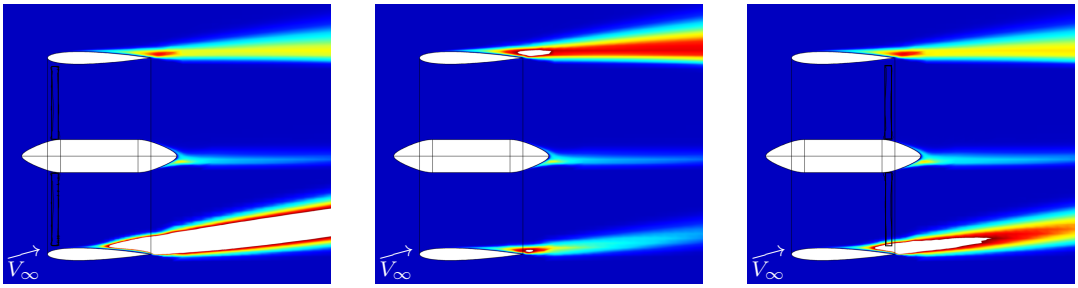

(a) Tractor (b) Wing (c) Pusher

Figure 12: Turbulent Viscosity Showing Differing Stall Characteristics between Each Configuration. Angle of Attack = 15 deg, T = 2.5 N, Re = 1.94×10^5, scale from blue ($\mu_t/\mu = 0$) to red ($\mu_t/\mu = 120$).

Figure 12 shows the effect of the propeller on the wing as stall is approached. Traub [17] noted that the top section of an annular wing stalls first, a phenomenon evident in Figure 12b. Figures 12a and 12c show the lower section stalling first as a result of the extra airflow forced through the wing. Furthermore, Figure 12c shows the pusher propeller is already starting to ingest highly turbulent flow, while the tractor propeller (Figure 12a) is still able to operate in relatively clean air.

6 Conclusion

This study shows that the position of the propeller inside an annular wing makes little difference to the steady state, non-stalled forward flight performance, though there is evidence to suggest that the pusher configuration requires less power to remain in steady flight than the tractor configuration. The presence of the propeller at moderate power is shown to delay stall, increasing $C_{L_{max}}$, though too much thrust can cause degradation in the performance of the wing. With increasing thrust, the aerodynamic centre is shown to shift aft.

As stall is approached, the tractor configuration is shown to be preferable, not suffering from ingesting the detached flow of the wing like the pusher configuration. Static thrust tests show the

pusher configuration to be preferable, producing more thrust for a given power despite a higher propeller clearance than the tractor configuration.

These tests were only conducted for one type of propeller and more investigation is required to ascertain if the propeller choice had an effect on the results. Additional variables not investigated here, such as the placements of guide vanes and control surfaces, should also be considered and may have a more profound effect than propeller placement in steady state, non-stalled forward flight.

7 Acknowledgements

The authours would like to thank Blake Formatti for the initial design and fabrication of the wind tunnel test model, Frank Buysschaert for his technical input and NUMECA for their support.

References

[1] J. Barlow, W. Rae, and A. Pope. *Low Speed Wind Tunnel Testing*. Wiley, 3rd edition, 1999.

[2] M. Drela. AVL. `http://web.mit.edu/drela/Public/web/avl/`.

[3] H. S. Fletcher. NACA Technical Note 4117: Experimental Investigation of Lift, Drag, and Pitching Moment of Five Annular Airfoils. Technical report, National Advisory Committee for Aeronautics, October 1957.

[4] W. Graf, J. Fleming, and W. Ng. Improving Ducted Fan UAV Aerodynamics in Forward Flight. In *46th AIAA Aerospace Sciences Meeting and Exhibit*, 2008.

[5] A. R. Kriebel, A. Sacks, and J.N. Nielsen. Theoretical Investigation of Dynamic Stability Derivatives of Ducted Propellers. Technical report, Bureau of Naval Weapons, US Navy, 1965.

[6] A. Maqsood and T. Go. Aerodynamic Estimation of Annular Wings Based on Leading-Edge Suction Analogy. *AIAA Journal*, 51(2):529–534, February 2013.

[7] M. Munk. NACA Report No. 151: General Biplane Theory. Technical report, National Advisory Committee for Aeronautics, 1923.

[8] NUMECA International. *User Manual: FINE/Marine v2*, March 2012.

[9] D. O'Brien. *Analysis of Computational Modeling Techniques for Complete Rotorcraft Configurations*. PhD thesis, Georgia Insititute of Technology, 2006.

[10] O. Ohanian. *Ducted Fan Aerodynamics and Modeling, with Applications of Steady and Synthetic Jet Flow Control*. PhD thesis, Virginia Polytechnic Institute and State University, 2011.

[11] L.P. Parlett. Aerodynamic Characteristics of a Small-Scale Shrouded Propeller at Angles of Attack from 0° to 90°. Technical Note TN3547, NACA, 1955.

[12] L. Prandtl. Induced Drag of Multiplanes. Technical Note 182, NACA, 1924.

[13] H. S. Ribner. The Ring Airfoil in Nonaxial Flow. *Journal of Aeronautical Sciences*, 14(9):529–530, 1947.

[14] A. Sacks and J. Burnell. Ducted Propellers - A Critical Review of the State of the Art. Technical report, Advanced Research Division of Hiller Aircraft Corporation, 1959.

[15] S. Shindo. Simplified Tunnel Correction Method. *Journal of Aircraft*, 32(1), 1995.

[16] P. Spalart and C. Rumsey. Effective Inflow Conditions for Turbulence Models in Aerodynamic Calculations. *AIAA Journal*, 45(10):2544–2553, 2007.

[17] L. W. Traub. Experimental Investigation of Annular Wing Aerodynamics. *Journal of Aircraft*, 46(3):988–996, May-June 2009.

[18] S. Yilmaz, D. Erdem, and M. Kavsaoglu. Effects of Duct Shape on a Ducted Propeller Performance. In *51st AIAA Aerospace Sciences Meeting including the New Horizons Forum and Aerospace Exposition*, 2013.